nano energy

RAPID COMMUNICATION

Superior electrochemical performance and structure evolution of mesoporous Fe$_2$O$_3$ anodes for lithium-ion batteries

CrossMark

Yunhua Xu[a,1], Guoqiang Jian[b,1], Yihang Liu[a], Yujie Zhu[a],
Michael R. Zachariah[a,b,*], Chunsheng Wang[a,**]

[a]Department of Chemical and Biomolecular Engineering, University of Maryland, College Park,
MD 20742, USA
[b]Department of Chemistry and Biochemistry, University of Maryland, College Park, MD 20742, USA

Abstract
Mesoporous Fe$_2$O$_3$ spherical particles with amorphous or crystalline structure were prepared at different temperatures using aerosol spray pyrolysis. The crystalline Fe$_2$O$_3$ (C-Fe$_2$O$_3$) anodes pyrolysized at 800 °C show better electrochemical performance than the amorphous Fe$_2$O$_3$ (A-Fe$_2$O$_3$) pyrolysized at 600 °C. Both, however, changed into nano-crystallite porous structure after charge/discharge cycles. The C-Fe$_2$O$_3$ spherical particles provided high reversible capacity of 800 mAh/g at 0.5 C over 300 charge/discharge cycles and retained 300 mAh/g at 10 C. The excellent cycling stability of the C-Fe$_2$O$_3$ spherical particles is mainly attributed to the interior voids in the mesoporous Fe$_2$O$_3$ particles that provide extra space to accommodate volume change and alleviate structural strain/stress during electrochemical reaction. The high rate performance of mesoporous Fe$_2$O$_3$ is attributed to (1) fast charge transfer reaction at the large interfacial area between electrode and liquid electrolyte, and (2) the reduced Li-ion diffusion distances. This study not only provides a simple synthesis method for lithium ion batteries, but also helps in designing novel and high performance electrode materials.
© 2013 Elsevier Ltd. All rights reserved.

Introduction

As the dominant power source in portable electronic devices, lithium-ion batteries (LIBs) are of great interest for potential application in emerging electric vehicles and renewable clean energy sources [1-3]. However, the low energy density of commercial graphite/LiCoO$_2$ lithium-ion batteries has

*Corresponding author. Tel.: +1 301 405 4311.
**Corresponding author. Tel.: +1 301 405 0352.
E-mail addresses: mrz@umd.edu (M.R. Zachariah),
cswang@umd.edu (C. Wang).
[1]These authors contributed equally to this work.

hampered implementation of a wide array of energy and environmentally desirous technologies [4,5]. In this regard, extensive efforts have been made to seek anode materials with high capacity, good rate capability, and long cycling life [1,6,7]. Iron is earth abundant, low cost, and nontoxic, making iron oxides a promising candidate for sustainable Li-ion batteries. Compared with conventional graphite anodes, Iron oxides (Fe_2O_3) have a three times higher theoretical capacity of 1006 mAh/g [6,7]. The large theoretical capacity of Fe_2O_3 is delivered by a conversion reaction where one chemical formula unit of Fe_2O_3 can react with 6 Li ions to form iron nano-particles dispersed in a Li_2O matrix [6,7]. However, the insertion/extraction of a large amount of Li ions leads to large volume change, which can adversely impact morphology and mechanical contact during reaction cycling, leading to a rapid decline in capacity.

One of the most successful methods to mitigate the volume change of Fe_2O_3 anodes is minimizing the particle size, i.e. nano-scale [1,7-12]. Pioneering work by Taroscon's group has demonstrated the significant improvement in cycle stability and rate capacity for nano-sized Fe_2O_3 particles in contrast to micro-sized particles [13,14]. The enhanced performance of nano-sized electrode materials in LIBs benefits from reduced structural strain/stress and improved charge/discharge kinetics. Following these ideas a variety of nano-Fe_2O_3 architectures, comprising nanoparticles, nanotubes to hierarchical nanostructures [15-35] have been synthesized using hydrothermal [26-28,31,32] and hard-template methods [15-17,30]. However, the large surface of Fe_2O_3 nanoparticles significantly increases irreversible capacity due to the formation of a large solid electrolyte interphase (SEI) during the first cycle. The large volume change of Fe_2O_3 during prolonged lithiation/delithiation cycles, resulting in cracking, followed by reformation and growth of the SEI films, and thus leading to low Coulombic efficiency and poor cycling stability. In addition, the Fe_2O_3 nano-particles have low tapping density, which reduces the active materials loading.

An appealing structure is mesoporous Fe_2O_3 particles, which not only take advantage of long cycling life and high rate performance of nano-Fe_2O_3 but also have high tapping density [36-38]. Specifically, mesoporous Fe_2O_3 particles with closed-mesopores have much smaller surface area than that of nanoparticles and open-pore materials, and thus offer high Coulombic efficiency and large taping density [39]. The nano-sized walls of the mesoporous Fe_2O_3 particles offer similar Li-ion diffusion pathway to Fe_2O_3 nanoparticles, which ensures fast kinetics and thus high rate capability. Finally, mesopores provide additional voids to effectively accommodate the volume change and alleviate the structural strain/stress during electrochemical reaction, improving the cycling stability. The advantages of mesoporous structure of electrodes for Li-ion batteries have been demonstrated in several conversion reaction electrodes, such as MnO_2 [40], Co_3O_4 [41,42], as well as Cr_2O_3 [43].

Mesoporous Fe_2O_3 particles with different morphologies have also been synthesized using complex acidic etching [27], template synthesis [30], hydrothermal synthesis [33], and chimie douce precipitation method [34]. The porous Fe_2O_3 particles prepared using these methods, however, can only sustain a short cycling life of 50-100 cycles [15-32]. There has been limited success in low-cost synthesis methods capable of mass production of mesoporous Fe_2O_3 with high cycling performance. Recently, aerosol spray pyrolysis has emerged as a powerful technique to synthesize nano-structured materials [44-47]. Aerosol spray pyrolysis is a simple process, whereby a precursor solution is atomized to form aerosol droplets dispersed in a carrier gas, which undergoes thermally-induced evaporation of solvent and solid-state chemical reactions to form the desired particles (Figure S1). Compared with wet-chemistry methods, aerosol spray pyrolysis has relatively low cost, and is compatible with on-line continuous production processes, thus providing a scalable manufacturing of particles. In a very recent work by our groups, ultrasmall and uniformly sized nano-Sn grain/carbon spheres were successfully produced using this technique [43]. It was shown that the rapid heating and cooling process associated with droplet formation and solvent evaporation can "freeze" the precursor solid particles to create uniformly nano-structured spherical particles, achievable by the wet chemistry methods.

In this paper, we employed a facile one-step "droplet-to-particle" aerosol spray pyrolysis method to produce crystalline or amorphous mesoporous Fe_2O_3 particles by tuning the pyrolysis temperatures. The electrochemical performance of the mesoporous Fe_2O_3 particles was investigated as anode materials in LIBs. High reversible capacity of $\sim$800 mAh/g at 0.5 C over 300 charge/discharge cycles were demonstrated for the crystalline Fe_2O_3 anode.

Experimental section

Synthesis of mesoporous Fe_2O_3 spherical particles

Mesoporous Fe_2O_3 particles were prepared by an aerosol spray pyrolysis method as illustrated in Figure S1. Typically, $\sim$3.2 g iron(III) nitrate nonahydrate ($Fe(NO_3)_3 \cdot 9H_2O$, Sigma-Aldrich) and 0.34 g sucrose ($C_{12}H_{22}O_{11}$, Sigma-Aldrich) were dissolved into 110 ml water. Aerosol droplets containing the dissolved precursors were generated using compressed air at a pressure of 0.24 MPa in a collision type atomizer. The geometric mean diameter of the droplets was measured to be $\sim$1 μm by a laser aerosol spectrometer. The produced aerosol droplets were firstly passed through a silica-gel diffusion dryer to remove most of the water, and then passed to a tube furnace at 600 or 800 °C. The normal residence time in the synthesis was around 1 s for a total gas flow rate of 3.5 L min^{-1}.The final products were collected on a 0.4 μm (pore size) HTTP Millipore filter.

Material characterizations

Scanning electron microscopy (SEM) and transmission electron microscopy (TEM) images were taken by Hitachi SU-70 analytical ultra-high resolution SEM (Japan) and JEOL 2100F field emission TEM (Japan), respectively. X-ray diffraction (XRD) pattern was recorded by Bruker Smart1000 (Bruker AXS Inc., USA) using CuKα radiation. BET specific surface area and pore size and volume were analyzed using N_2 absorption with Micromeritics ASAP 2020 Porosimeter Test Station.

Electrochemical measurements

The mesoporous Fe_2O_3 anodes were mixed with carbon black and sodium carboxymethyl cellulose (CMC) binder to form slurry at the weight ratio of 70:15:15. The electrode was prepared by casting the slurry onto copper foil with active material loading of ~1.0 mg/cm^2 using a doctor blade and dried in a vacuum oven at 100 °C overnight. Coin cells were assembled with lithium foil as the counter electrode, 1 M LiPF$_6$ in a mixture of ethylene carbonate/diethyl carbonate (EC/DEC, 1:1 by volume) as the electrolyte, and Celgard®3501 (Celgard, LLC Corp., USA) as the separator. Electrochemical performance was tested using Arbin battery test station (BT2000, Arbin Instruments, USA). Rate capability was examined by charging/discharging at different rates from 0.1 C to 30 (C rate = 1006 mA/g). Cyclic voltammogram scanned at 0.1 mV/s between 0–3 V was recorded using Solatron 1260/1287 Electrochemical Interface (Solartron Metrology, UK). For comparison, the commercial Fe_2O_3 nanoparticles with particle size of 50 nm (Sigma-Aldrich) were examined at the same cell assemble and test conditions. Galvanostatic intermittent titration technique (GITT) measurement was carried out by applying a pulse constant current of 200 mA/g with duration of 30 min and followed by 6 h relaxation to reach an equilibrium voltage.

Results and discussion

A schematic illustration for the preparation of mesoporous Fe_2O_3 nanospheres is presented in Figure S1. The aerosol spray pyrolysis synthesis followed a one-step "droplet-to-particle" process whereby precursor solutions are atomized and thermally decomposed to form mesoporous particles. The key to the formation of the closed-mesopore structure is the existence of the gas blowing agent in the precursor solution. Both decomposition of nitrate salts and oxidation of sucrose could produce gases which lead to the formation of porous structure. The role of sucrose here is to increase the gas production in the sintering process, as illustrated in Figure S1. Two temperatures, 600 °C and 800 °C, were used to synthesis mesoporous Fe_2O_3 spheres, and denoted as A-Fe_2O_3 (amorphous) and C-Fe_2O_3 (crystalline), respectively. The morphology of Fe_2O_3 spheres was illustrated in the SEM images in Figure 1. Spherical shape of the precursor

droplets was well preserved for both samples of A-Fe_2O_3 and C-Fe_2O_3, which is the typical feature of materials synthesized by aerosol spray pyrolysis. The Fe_2O_3 spherical particles for both samples are distributed in the diameter range of hundreds of nanometers. The enlarged SEM image in Figure 1c clearly reveals open and uniformly distributed nano-sized pores on the surface of the Fe_2O_3 spherical particles.

The mesoporous nature within the Fe_2O_3 spheres is evidenced by TEM images in Figure 2. For both samples of A-Fe_2O_3 and C-Fe_2O_3, the porous structure is clearly revealed with the contrast between Fe_2O_3 walls and mesopores in the TEM images. The lighter regions represent pores, while the darker represent Fe_2O_3 walls. Both the diameter of pores and the thickness of the Fe_2O_3 walls are around 10 nm. C-Fe_2O_3 shows much stronger contrast and better-defined pore structure than A-Fe_2O_3. At higher temperature of 800 °C, much faster and complete decomposition of the precursors occurred, facilitating formation of crystal structure and well-defined pores (Figure 2f and g); while A-Fe_2O_3 particles show an amorphous structure (Figure 2c). This is further confirmed by the selected area electron diffraction (SAED) images (Figure 2d and h). Bright diffraction rings are presented for C-Fe_2O_3 (Figure 2h), which is a typical feature of a crystalline structure. Figure 2g shows the high-resolution TEM lattice image. The lattice spacing was measured to be 0.37 nm, which is in good agreement with the d-spacing of the (012) plane of crystalline Fe_2O_3. However, only broad diffraction rings are observed for A-Fe_2O_3 (Figure 2d), indicating an amorphous structure. The structures of both A-Fe_2O_3 and C-Fe_2O_3 were also characterized using X-ray diffraction (XRD) (Figure S2). Fine diffraction peaks were displayed for C-Fe_2O_3, which can be indexed to the crystal structure of Fe_2O_3 (JCPDS card no.: 33-0664). No impurity peaks were detected, indicating that the thermal decomposition at the synthesis temperature (800 °C) is sufficient to form crystal Fe_2O_3, even though the heating time is as short as a few seconds. In contrast, no diffraction peaks are displayed for A-Fe_2O_3, which is in good agreement with the high-resolution TEM and SAED results (Figure 2c, d, g and h).

The closed-mesopore structure of the Fe_2O_3 spheres was analyzed using nitrogen absorption measurements. Figure S3 shows the adsorption isotherm. The Brunauer–Emmett–Teller (BET) specific surface area and pore volume are 23 m^2/g and 0.015 cm^3/g for A-Fe_2O_3, 58 m^2/g and
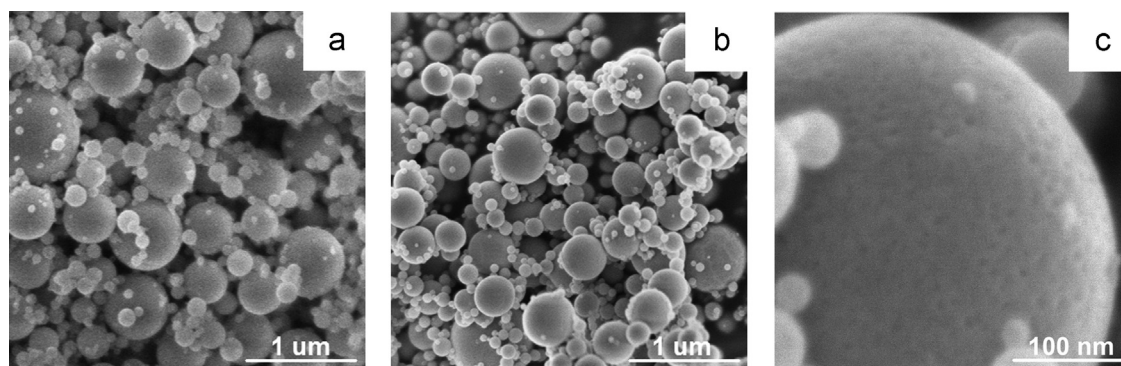
Figure 1 SEM images of (a) A-Fe_2O_3 and (b,c) C-Fe_2O_3.
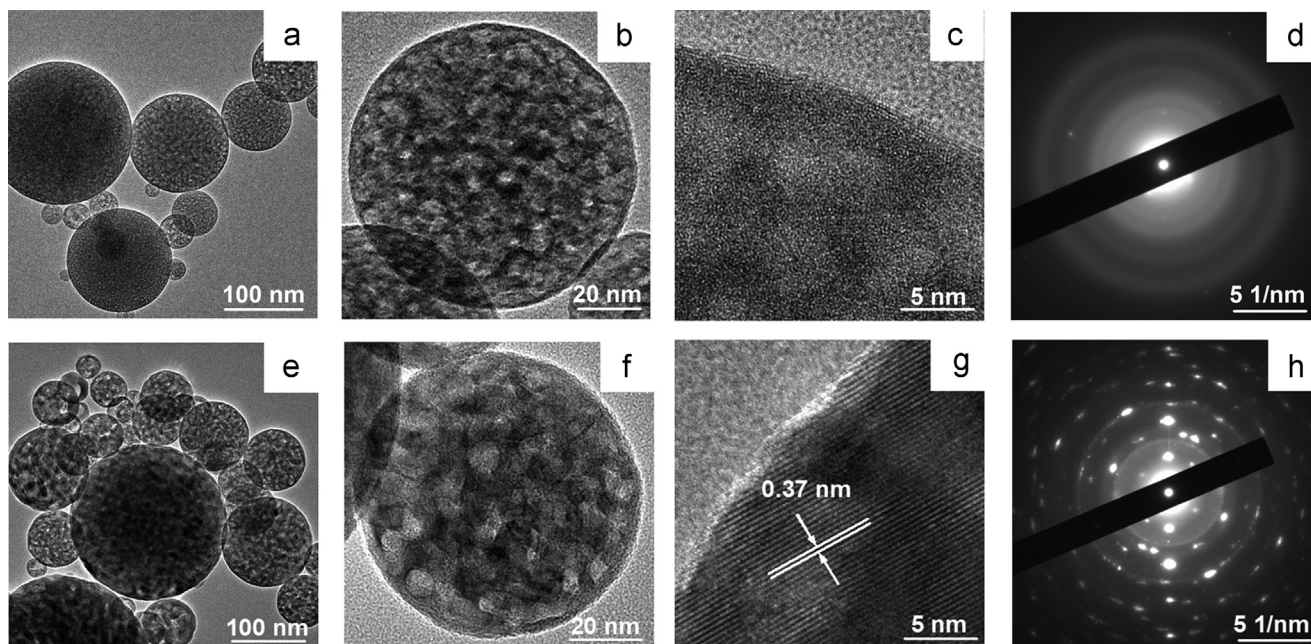
Figure 2 TEM images of (a–c) A-Fe$_2$O$_3$ and (e–g) C-Fe$_2$O$_3$. SAED images of (d) A-Fe$_2$O$_3$ and (h) C-Fe$_2$O$_3$.

0.15 cm^3/g for C-Fe$_2$O$_3$, respectively. The surface areas of both A-Fe$_2$O$_3$ and C-Fe$_2$O$_3$ are much smaller than reported porous Fe$_2$O$_3$ anodes (103-207 m^2/g for mesoporous Fe$_2$O$_3$ cocoons and rods [34] and 765.0 m^2/g for porous Fe$_2$O$_3$ nanotubes [17]). BJH average open-pore diameter is 10 nm and 11 nm for A-Fe$_2$O$_3$ and C-Fe$_2$O$_3$, respectively, which are in consistence with the results by TEM images.

Electrochemical performance of both A-Fe$_2$O$_3$ and C-Fe$_2$O$_3$ electrodes was investigated in coin cells using lithium as the counter electrode. Figure 3a and b show the first two cyclic voltammogram (CV) scans of A-Fe$_2$O$_3$ and C-Fe$_2$O$_3$ at a scan rate of 0.1 mV/s between 0 V and 3.0 V. The strong reduction peaks at 0.65 V for C-Fe$_2$O$_3$ and 0.7 V for A-Fe$_2$O$_3$ in the first cycle are attributed to the conversion reaction from Fe^{3+} to Fe^0. In the second cycle, both peaks shifted to higher voltage of 0.9 V for C-Fe$_2$O$_3$ and 0.8 V for A-Fe$_2$O$_3$ with reduced peak current. The current peak shift to more positive potential in the second cycle is a common phenomenon for iron oxide anodes observed by others [15-35] and was attributed to the structure changes during the lithium insertion in the first cycle. The higher peak current in the first lithiation was partially attributed to the formation of solid-electrolyte interface (SEI) films. In the anodic process, similar oxidation curves and peak intensity were presented for A-Fe$_2$O$_3$ and C-Fe$_2$O$_3$ in the first cycle with two broad peaks centered at 1.65 V and 1.85 V, respectively, accounting for the oxidation reaction from Fe^0 to Fe^{3+}. Meanwhile, no significant difference between the first and second anodic scans was observed for both electrodes.

The difference between crystalline and amorphous Fe$_2$O$_3$ can also be observed in galvanic charge/discharge curves. Figure 3c and d illustrates the first three charge/discharge curves of A-Fe$_2$O$_3$ and C-Fe$_2$O$_3$ at 100 mA/g from 0 to 3.0 V. The crystalline Fe$_2$O$_3$ showed a long and flat plateau at 0.8 V in the first discharge (Figure 3d), and then shifts to 1.0 V and became a slop line in the subsequent discharges; while the discharge potential profile of amorphous Fe$_2$O$_3$ in the first discharge is less flat than that of crystalline Fe$_2$O$_3$ (a typical feature for amorphous electrode materials [48,49]), and maintain its slope shape but slightly shifted to a higher potential in the following discharges. Similar to the CV curves, potential increase in the second cycles for crystalline Fe$_2$O$_3$ have been widely reported for iron oxide and other anode materials [7,14,50] and were attributed to the structure changes during the lithium insertion in the first cycle. In the first cycle, the volume change due to the conversion reaction produced defects although the mesoporous released some stress/strain and changed the Fe$_2$O$_3$ from crystal or amorphous network structure to nano-crystallite structure, which would facilitate the lithium ion insertion and lower the electrochemical polarization in the subsequent cycles [7]. The nano-crystallite structure after lithiation/delithation cycles was confirmed by the TEM and SAED images after 100 cycles (Figure 4).

During delithiation, a plateau-like potential slope at 1.2-2.5 V was observed (Figure 3c and d), which accounts for the oxidation reaction of Fe^0-Fe^{3+}. There is no obvious difference in the charge processes for the first three cycles. The almost identical charge/discharge behavior from the second cycle demonstrates good reversibility and stability of the mesoporous Fe$_2$O$_3$ anodes.

The first discharge of C-Fe$_2$O$_3$ delivered a capacity of 1365 mAh/g, much higher than the theoretical value of 1006 mAh/g. The extra capacity is attributed to the decomposition reaction of the electrolyte. The reversible capacity of C-Fe$_2$O$_3$ in the first cycle is 1003 mAh/g, corresponding to 99.7% of the theoretical capacity. The high reversible capacity identifies full utilization of the porous Fe$_2$O$_3$ through the whole spherical particles. No capacity fading occurred in the following cycles, revealing good stability. In contrast, A-Fe$_2$O$_3$ delivered higher charge and discharge capacities of 1167 mAh/g and 1501 mAh/g, respectively. The higher capacity could be associated with the amorphous structure.
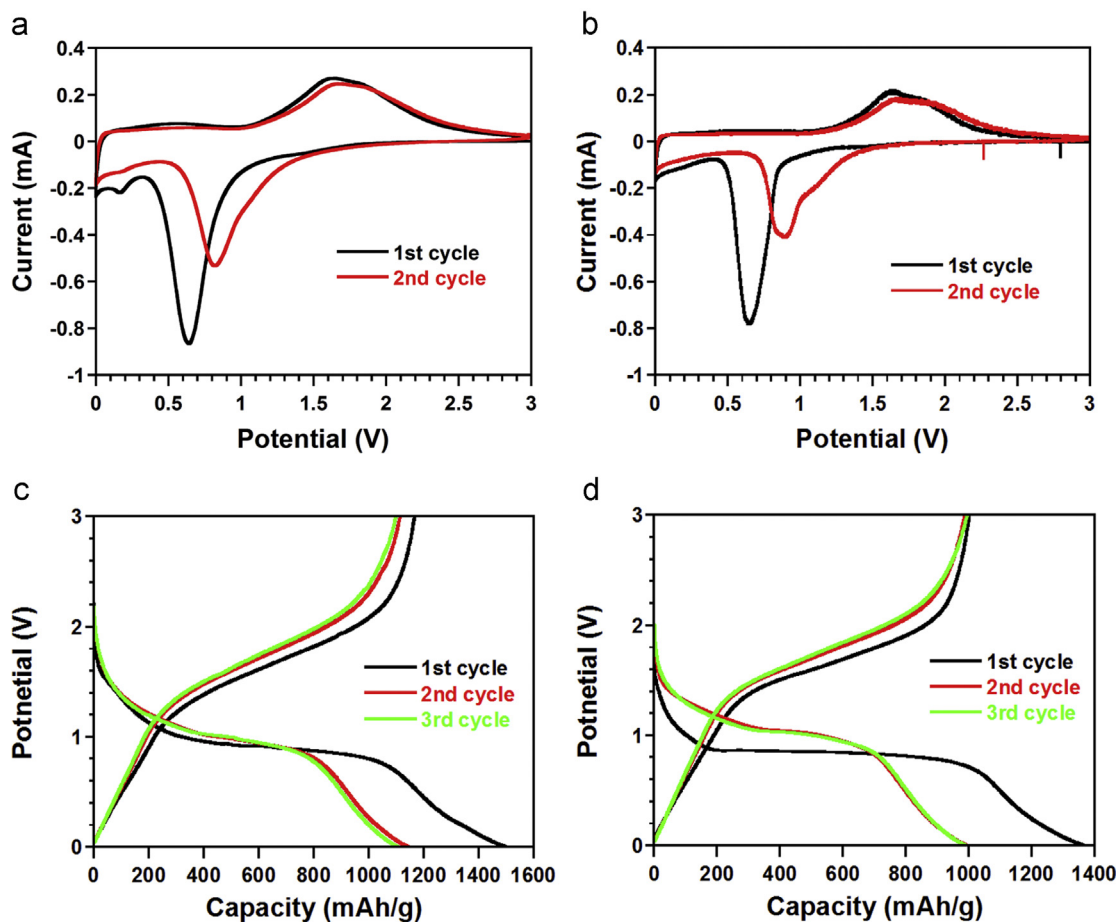
Figure 3 Cyclic voltammograms of (a) A-Fe_2O_3 and (b) C-Fe_2O_3 in the initial two cycles scanned between 0–3 V at a rate of 0.1 mV/s, and charge/discharge profiles of (c) A-Fe_2O_3 and (d) C-Fe_2O_3 at the initial three cycles at 100 mA/g and 0–3 V.

The CVs in Figure 3 and images in Figure 4 show that the structure change from crystal or amorphous to nano-crystallite in the first charge/discharge cycle influences the electrochemical behavior (equilibrium potential and overpotential) in the following cycles. To understand how the structure change influences the thermodynamic equilibrium potential and kinetic overpotential of the mesoporous Fe_2O_3 electrodes, GITT technique was used to investigate the equilibrium potential and overpotential of the Fe_2O_3 anodes in the first two charge/discharge cycles. The GITT curves are shown in Figure S4. Since the capacity of A-Fe_2O_3 is larger than C-Fe_2O_3 (Figure 3c and d), the capacities were normalized to the state of discharge (SOD) to obtain the intrinsic electrochemical property. Figure 5 compares the equilibrium potentials and overpotentials of C-Fe_2O_3 and A-Fe_2O_3 in the initial two cycles. In the first cycle (Figure 5a), the initial discharge equilibrium potential of the crystalline Fe_2O_3 is slightly lower than that of amorphous Fe_2O_3 but reaches similar value after 50% of discharge. Charge equilibrium potentials of the two Fe_2O_3 electrodes appear similar, implying that the structure change occurred in the early stage of the first discharge. In the second cycle, both C-Fe_2O_3 and A-Fe_2O_3 show the same charge/discharge equilibrium potential because both crystalline and amorphous Fe_2O_3 were altered into nano-crystallite structure in the first cycle. The overpotentials of both C-Fe_2O_3 and A-Fe_2O_3 decrease

with SOD but the amorphous Fe_2O_3 shows a slightly larger value than that of the crystalline Fe_2O_3 at the beginning of the first discharge, indicating that the structure change from amorphous to nano-crystallite is more difficultly than from crystalline to nano-crystallite. The discharge overpotentials for the two Fe_2O_3 electrodes in the second charge/discharge cycles are similar and much lower than those in the first cycle. Therefore the formation of nano-crystallite structure enhanced the lithiation/delithiation kinetics of Fe_2O_3 electrodes.

The cycling stability of both C-Fe_2O_3 and A-Fe_2O_3 electrodes were investigated by repeated charge/discharge processes between 0 and 3.0 V at a current density of 500 mA/g, as shown in Figure 6a. Commercial Fe_2O_3 nanoparticles with an average particle size of 50 nm were also examined at the same conditions for comparison. C-Fe_2O_3 provides a charge capacity of around 1000 mAh/g in the first cycle follow by slight capacity decay for 15 cycles, and then remains stable at ~800 mAh/g up to 100 cycles. However, the capacity of A-Fe_2O_3 continuously drops to and then stabilizes at ~450 mAh/g, which is only half of the capacity of C-Fe_2O_3. Although both C-Fe_2O_3 and A-Fe_2O_3 altered into the similar nano-crytallite structure after the first cycle, the large overpotential of amorphous A-Fe_2O_3 in the first lithiation (Figure 5c) implies that more severe structure deformation occurred during the first lithiation, which
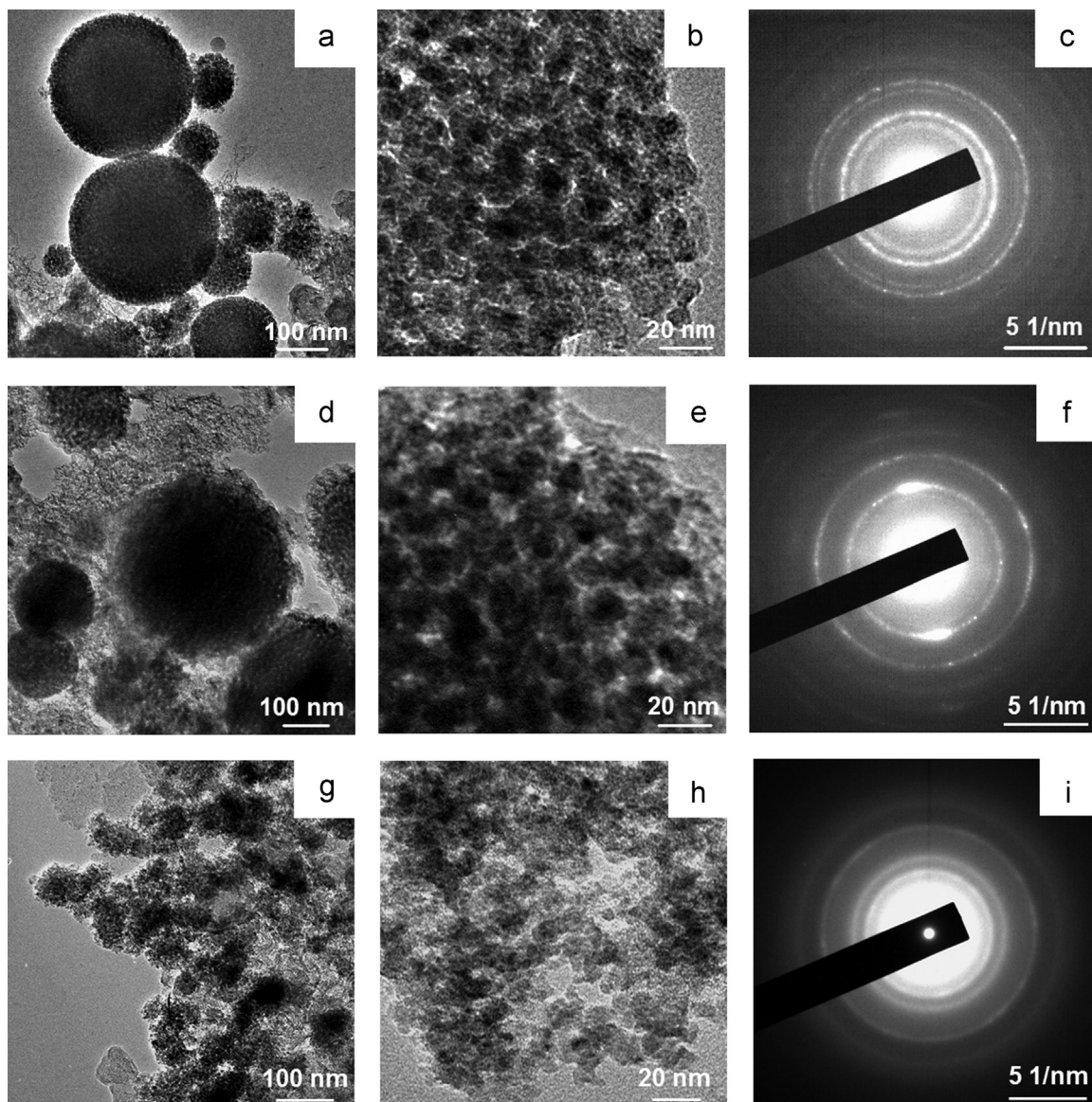
Figure 4 TEM images of (a,b) A-Fe$_2$O$_3$, (d,e) C-Fe$_2$O$_3$ and (g,h) commercial Fe$_2$O$_3$ nanoparticles, and SAED images of (c) A-Fe$_2$O$_3$, (f) C-Fe$_2$O$_3$ and (i) commercial Fe$_2$O$_3$ nanoparticle anodes taken after 100 cycles.

reduces the cycling stability. The commercial Fe$_2$O$_3$ nanoparticles provided similar capacity in the initial cycles, but subsequently showed a rapid decay to failure after ~50 cycles (Figure 6a). These results clearly demonstrate that the superior cycling performance of the mesoporous C-Fe$_2$O$_3$ synthesized using aerosol spray pyrolysis over the commercial nanoparticles.

The material structure of the mesoporous Fe$_2$O$_3$ anodes and the commercial nanoparticles after 100 charge/discharge cycles between 0 and 3.0 V at 500 mA/g current were investigated using TEM (Figure 4). Both A-Fe$_2$O$_3$ and C-Fe$_2$O$_3$ maintain the integrity of the spherical particles. High resolution TEM images (Figure 4b and e) revealed that the porous structure also survived the lithium ion insertion/extraction reactions for both anodes. In comparison to the porous structure with a wall-frame network of the unreacted Fe$_2$O$_3$ spherical particles in Figure 2, the porous Fe$_2$O$_3$ spheres were converted into more loosed porous

structure. The diameter of nanoparticles is still around 10 nm and the preservation of the spherical morphology, demonstrating that the mesoporous Fe$_2$O$_3$ spheres can effectively accommodate the volume change, and alleviate the strain during the electrochemical cycles. As shown in the SAED images of Fe$_2$O$_3$ particles after 100 cycles in Figure 4c and f, crystal pattern was displayed for both A-Fe$_2$O$_3$ and C-Fe$_2$O$_3$ anodes. In contrast to the porous Fe$_2$O$_3$, the commercial nanoparticles suffered much more severe structure and morphology deformation during the charge/discharge cycles as evidenced by the TEM images in Figure 4 and Figure S5. After cycles, the spherical morphology was destroyed, which is consistent with the worse cycling stability.

Due to the high cycling stability of C-Fe$_2$O$_3$, the extended cycling behavior of C-Fe$_2$O$_3$ was further evaluated at 500 mA/g after three cycles at 100 mA/g (Figure 6b). After 300 cycles, no capacity fading occurred with capacity
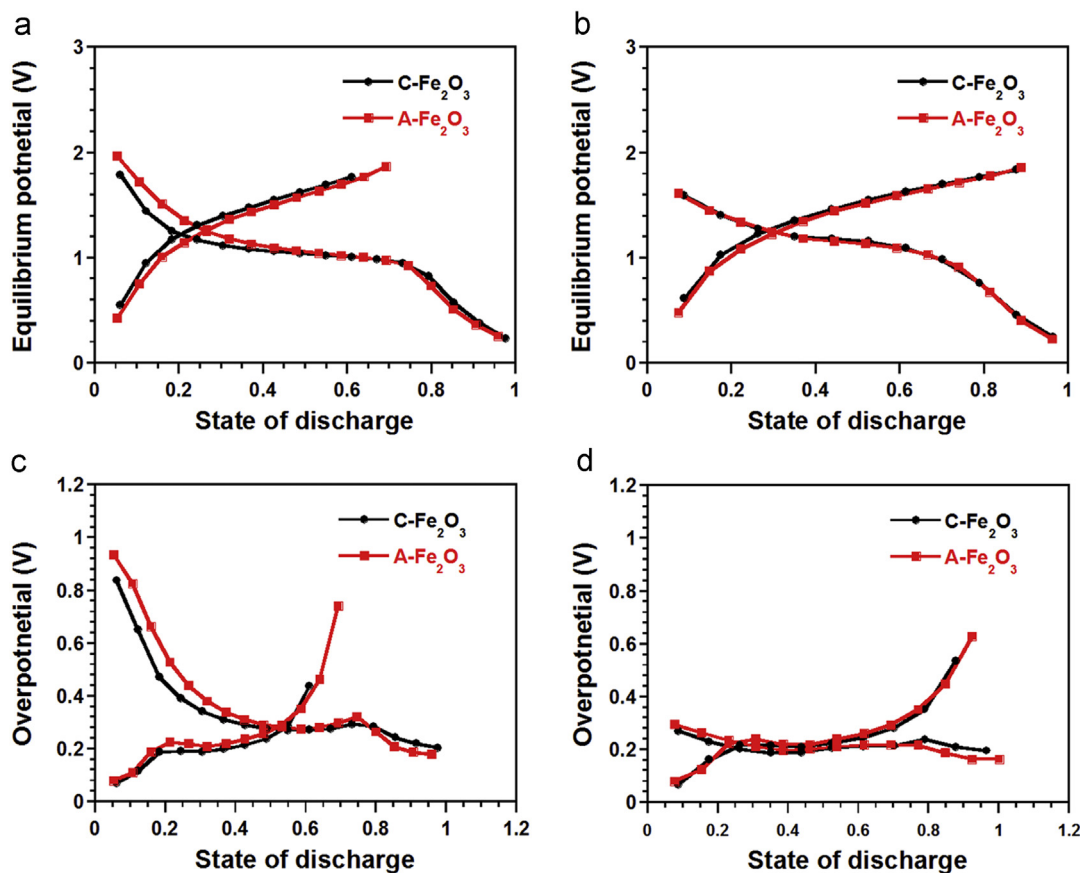
Figure 5 Equilibrium charge/discharege profiles of the mesoporous Fe_2O_3 anodes in the (a) first and (b) second cycles. Overpotential of the mesoporous Fe_2O_3 in the (c) first and (d) second cycles.

retention of ~800 mAh/g. Such long-life cycling performance has barely been reported in literature [15-34]. The Coulombic efficiency is approaching 100% over the 300 cycles. These definitely prove that the mesoporous Fe_2O_3 sphere electrode synthesized at 800 °C is a promising material for energy storage and rechargeable batteries.

The rate capability of the mesoporous C-Fe_2O_3 anodes was examined at different current densities. Excellent rate performance of the mesoporous C-Fe_2O_3 anodes was demonstrated in Figure 6c. A high capacity of 300 mAh/g was retained at a 10 C rate (C rate=1006 mA/g), which is comparable to graphite used in commercial lithium ion batteries. Even at a higher rate of 20 C, the capacity retention is still as high as 120 mAh/g, which is much better than those previously reported solid iron oxide nanoparticles [18]. Remarkably, the rate capability of the mesoporous C-Fe_2O_3 anodes is superior to that of those conductive additive-incorporated iron oxide anodes, such as amorphous carbon, graphene as well as carbon nanotubes [31,51-53]. The excellent rate capability is believed to be associated with the mesoporous structure.

Clearly, the unique porous spherical structure of the mesoporous Fe_2O_3 anodes is responsible for the enhanced electrochemical performance. As is well known, the porous structure provides extra space to accommodate the large volume change during lithium ion insertion/extraction, which helps alleviate the absolute strain on the surface

and avoid mechanical crack and maintains the integrity of the whole particle and good electric pass within the spherical particles, and thus improving the cycling stability and rate performance. In addition, the reduced dimension of Fe_2O_3 electrode (nano-sized walls) not only offers further assistance to reduce the strain led by lithiation/delithiation reaction, but also provides short transport distances for lithium ions and electrons, allowing fast kinetics. Along with the nano-sized dimension, this porous spherical structure enables an excellent rate capability. Finally, compared with amorphous structure, the crystal structure is another factor to provide a strong mechanical support. As a result, the mesoporous crystalline Fe_2O_3 spheres not only enable full utilization of Fe_2O_3 to store lithium ions, thus providing high capacity, but also improve the cycling stability and rate capability.

Conclusion

Mesoporous Fe_2O_3 spherical particles were synthesized at different temperatures of 600 °C and 800 °C using aerosol spray pyrolysis as anode materials for lithium-ion batteries. A-Fe_2O_3 is amorphous, while C-Fe_2O_3 has a fine crystal structure. High capacity, good cycling stability as well as excellent rate capability were demonstrated for C-Fe_2O_3. The TEM results revealed that the electrochemical cycles converted the wall-frame porous structure into nano-crystallite
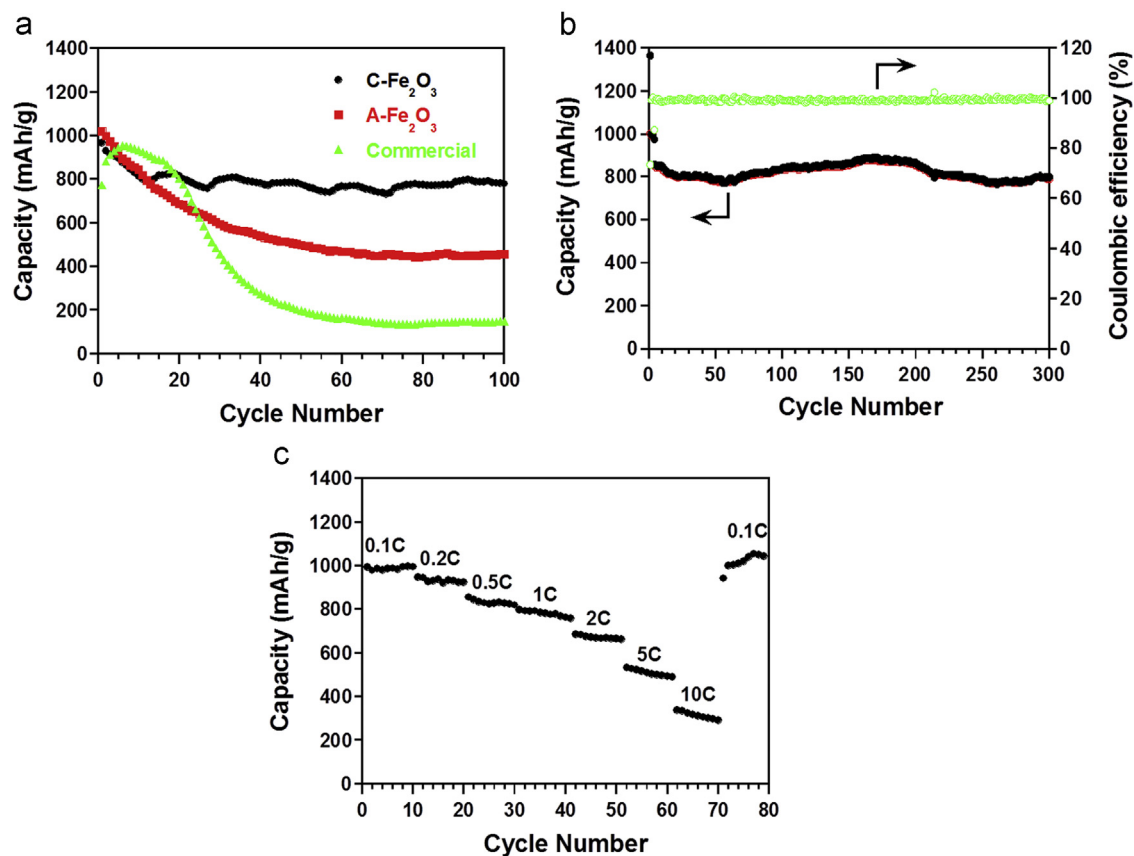
Figure 6 (a) Comparison of cycling performance of A-Fe$_2$O$_3$, C-Fe$_2$O$_3$ and commercial Fe$_2$O$_3$ nanoparticles. (b) Cycling performance of C-Fe$_2$O$_3$ at 500 mA/g and 0–3 V after three cycles at 100 mA/g. (c) Rate capability of C-Fe$_2$O$_3$.

structure for both crystalline and amorphous Fe$_2$O$_3$. The better stability of C-Fe$_2$O$_3$ suggests that mesoporous crystal structure is promising for high performance anode materials in LIBs. Our study not only provides a simple synthesis method for lithium ion batteries, but also helps in designing novel and high performance electrode materials.

Acknowledgments

Appendix A.   Supporting information

Supplementary data associated with this article can be found in the online version at http://dx.doi.org/10.1016/j.nanoen.2013.10.003.

References

[1] U. Kasavajjula, C.S. Wang, A.J. Appleby, J. Power Sources 163 (2007) 1003-1039.
[2] B. Dunn, H. Kamath, J.-M. Tarascon, Science 334 (2011) 928-935.
[3] Z. Yang, J. Zhang, M.C.W. Kintner-Meyer, X. Lu, D. Choi, J.P. Lemmon, J. Liu, Chem. Rev. 111 (2011) 3577-3613.
[4] J.R. Dahn, T. Zheng, Y. Liu, J.S. Xue, Science 270 (1995) 590-593.
[5] M.S. Dresselhaus, Adv. Phys. 30 (1981) 139-326.
[6] J. Cabana, L. Monconduit, D. Larcher, M.R. Palacín, Adv. Mater. 22 (2010) E170-E192.
[7] P. Poizot, S. Laruelle, S. Grugeon, L. Dupont, J.-M. Tarascon, Nature 407 (2000) 496-499.
[8] X.W. Lou, L.A. Archer, Z. Yang, Adv. Mater. 20 (2008) 3987-4019.
[9] A.S. Aricò, P. Bruce, B. Scrosati, J.-M. Tarascon, W.V. Schalkwijk, Nat. Mater. 4 (2005) 366-377.
[10] Y.-G. Guo, J.-S. Hu, L.-J. Wan, Adv. Mater. 20 (2008) 2878-2887.
[11] P.G. Bruce, B. Scrosati, J.-M. Tarascon, Angew. Chem. Int. Ed. 47 (2008) 2930-2946.
[12] M.-K. Song, S. Park, F.M. Alamgir, J. Cho, M. Liu, Mater. Sci. Eng. R 72 (2011) 203-252.
[13] D. Larcher, C. Masquelier, D. Bonnin, Y. Chabre, V. Masson, J.-B. Leriche, J.-M. Tarascon, J. Electrochem. Soc. 150 (2003) A133-A139.
[14] D. Larcher, D. Bonnin, R. Cortes, I. Rivals, L. Personnaz, J.-M. Tarascon, J. Electrochem. Soc. 150 (2003) A1643-A1650.
[15] J. Chen, L. Xu, W. Li, X. Gou, Adv. Mater. 17 (2005) 582-586.
[16] Z. Wang, D. Luan, S. Madhavi, C.M. Li, X.W. Lou, Chem. Commun. 47 (2011) 8061-8063.
[17] N. Kang, J.H. Park, J. Choi, J. Jin, J. Chun, I.G. Jung, J. Jeong, J.-G. Park, S.M. Lee, H.J. Kim, S.U. Son, Angew. Chem. Int. Ed. 51 (2012) 6626-6630.

[18] Y.-M. Lin, P.R. Abel, A. Heller, C.B. Mullins, J. Phys. Chem. Lett. 2 (2011) 2885–2891.
[19] P. Tartaj, J.M. Amarilla, J. Power Sources 196 (2011) 2164–2170.
[20] G.F. Ortiz, I. Hanzu, P. Lavela, J.L. Tirado, P. Knauth, T. Djenizian, J. Mater. Chem. 20 (2010) 4041–4046.
[21] S. Chaudhari, M. Srinivasan, J. Mater. Chem. 22 (2012) 23049–23056.
[22] H.S. Kim, Y. Piao, S.H. Kang, T. Hyeon, Y.E. Sung, Electrochem. Commun. 12 (2010) 382–385.
[23] J.S. Zhou, H.H. Song, X.H. Chen, L.J. Zhi, S.Y. Yang, J.P. Huo, W.T. Yang, Chem. Mater. 21 (2009) 2935–2940.
[24] J. Zhong, C. Cao, Y. Liu, Y. Li, W.S. Khan, Chem. Commun. 46 (2010) 3869–3871.
[25] S.-L. Chou, J.-Z. Wang, Z.-X. Chen, H.-K. Liu, S.-X. Dou, Nanotechnology 22 (2011) 265401.
[26] B. Wang, J.S. Chen, H.B. Wu, Z. Wang, X.W. Lou, J. Am. Chem. Soc. 133 (2011) 17146–17148.
[27] J.S. Chen, T. Zhu, X.H. Yang, H.G. Yang, X.W. Lou, J. Am. Chem. Soc. 132 (2010) 13162–13164.
[28] L. Zhang, H.B. Wu, S. Madhavi, H.H. Hng, X.W. Lou, J. Am. Chem. Soc. 134 (2012) 17388–17391.
[29] B. Koo, H. Xiong, M.D. Slater, V.B. Prakapenka, M.P. Podsiadlo, C.S. Johnson, T. Rajh, E.V. Shevchenko, Nano Lett. 12 (2012) 2429–2435.
[30] X. Xu, R. Cao, S. Jeong, J. Cho, Nano Lett. 12 (2012) 4988–4991.
[31] Y. Ma, G. Ji, J.Y. Lee, J. Mater. Chem. 21 (2011) 13009–13014.
[32] Y. Han, Y. Wang, L. Li, Y. Wang, L. Jiao, H. Yuan, S. Liu, Electrochim. Acta 56 (2011) 3175–3181.
[33] J. Zhang, Y. Sun, Y. Yao, T. Huang, A. Yu, J. Power Source 222 (2013) 59–65.
[34] W.A. Ang, N. Gupta, R. Prasanth, S. Madhavi, ACS Appl. Mater. Interfaces 4 (2012) 7011–7019.
[35] X. Jia, J.-J. Chen, J.-H. Xu, Y.-N. Shi, Y.-Z. Fan, M.-S. Zheng, Q.-F. Dong, Chem. Commun. 48 (2012) 7410–7412.
[36] Y. Ren, A.R. Armstrong, F. Jiao, P.G. Bruce, J. Am. Chem. Soc. 132 (2010) 996–1004.
[37] F. Jiao, J. Bao, P.G. Bruce, Electrochem. Solid-State Lett. 10 (2007) A264–A266.
[38] Y. Ren, Z. Ma, P.G. Bruce, Chem. Soc. Rev. 41 (2012) 4909–4927.
[39] J.C. Guo, Q. Liu, C.S. Wang, M.R. Zachariah, Adv. Funct. Mater. 22 (2012) 803–811.
[40] J.-Y. Luo, J.-J. Zhang, Y.-Y. Xia, Chem. Mater. 18 (2006) 5618–5623.
[41] K.M. Shaju, F. Jiao, A. Débart, P.G. Bruce, Phys. Chem. Chem. Phys. 9 (2007) 1837–1842.
[42] Y. Li, B. Tan, Y. Wu, Nano Lett. 8 (2008) 265–270.
[43] L. Dupont, S. Laruelle, S. Grugeon, C. Dickinson, W. Zhou, J.-M. Tarascon, J. Power Sources 175 (2008) 502–509.
[44] Y.H. Xu, Q. Liu, Y.J. Zhu, Y.H. Liu, A. Langrock, M.R. Zachariah, C.S. Wang, Nano Lett. 13 (2013) 470–474.
[45] A. Langrock, Y.H. Xu, Y.H. Liu, A. Manivannan, C.S. Wang, J. Power Sources 223 (2013) 62–67.
[46] A. Prakash, A.V. McCormick, M.R. Zachariah, Chem. Mater. 16 (2004) 1466–1471.
[47] G.Q. Jian, L. Liu, M.R. Zachariah, Adv. Funct. Mater. 23 (2013) 1341–1346.
[48] Y. Yin, Y. Hu, P. Wu, H. Zhang, C. Cai, Chem. Commun. 48 (2012) 2137–2139.
[49] Y.-L. Liu, Y.H. Xu, X.G. Han, C. Pellegrinelli, Y.J. Zhu, H.L. Zhu, J.Y. Wan, A.C. Chung, O. Vaaland, C.S. Wang, L.B. Hu, Nano Lett. 12 (2012) 5664–5668.
[50] C. Chan, H. Peng, G. Liu, K. McIlwrath, X.F. Zhang, R.A. Huggins, Y. Cui, Nat. Nanotechnol. 3 (2008) 31–35.
[51] S.-L. Chou, J.-Z. Wang, D. Wexler, K. Konstantinov, C. Zhong, H.-K. Liu, S.-X. Dou, J. Mater. Chem. 20 (2010) 2092.
[52] X. Zhu, Y. Zhu, S. Murali, M.D. Stoller, R.S. Ruoff, ACS Nano 4 (2011) 3333–3338.
[53] W.-J. Yu, P.-X. Hou, F. Li, C. Liu, J. Mater. Chem. 22 (2012) 13756–13763.
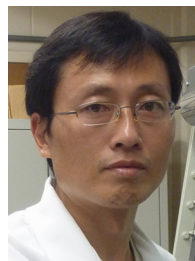
Yunhua Xu received his Ph.D. degree in Materials Physics and Chemistry from South China University of Technology in 2008 and was a visiting student and then postdoctoral fellow in the Center for Polymers and Organic Solids at the University of California, Santa Barbara from 2006 to 2009. He moved to University of Maryland, College Park in 2009 and is currently an Assistant Research Scientist. His research interests focus on electrode materials and electrochemistry for rechargeable batteries, including Li-ion and Na-ion batteries.

Guoqiang Jian is currently a Ph.D. candidate in Prof. Zachariah's group at University of Maryland, College Park. He received his B.S. and M.S. degrees in Chemistry from Nanjing University, China. His current research interests are mainly on high temperature chemistry of nanomaterials and aerosol synthesis of functional nanomaterials and their applications in nanoenergetics and lithium ion batteries. He is a recipient of William F. Bailey Summer Research Award and Dean's List Awards for Significant Publication Records and Scholastic Excellence at University of Maryland.
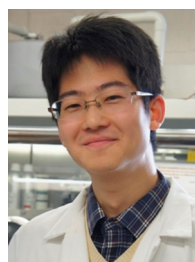
Yihang Liu received a master degree in Chemical Engineering from University of Maryland, College Park, US and a bachelor degree in opto-electronic Engineering from Beijing Institute of Technology, China. His research interests are energy storage devices, including Li-ion and Na-ion batteries.

Yujie Zhu received his B.S. degree in Chemical Engineering from Tsinghua University, and earned his Ph.D. degree in Chemical and Biomolecular Engineering in 2013 from University of Maryland, College Park (UMCP). He is now a postdoctoral research associate in Professor Chunsheng Wang's research group at UMCP. His research focuses on development of electrochemical techniques for phase transition electrode materials, investigation of charge/discharge process for single particle systems by in situ transmission electron microscopy, and electrode materials synthesis for lithium-/sodium-ion batteries.

Professor Zachariah is the founding Director of the University of Maryland/NIST Center for NanoManufacturing and Metrology and was the founding Director of the Army Center for Nanoenergetics Research. He received his Ph.D. in Chemical Engineering from UCLA and is a Professor of Chemical Engineering and Chemistry at the University of Maryland. His research has focused on the aerosol dynamics and materials synthesis. He has also published extensively on the metrology of nanoparticles in both the liquid and gas phases. This includes the development of new mass-spectrometry and ion-mobility methods to characterize nanoparticles and their reactivity. He is a recipient of the University of Maryland Outstanding Researcher Award, and the Sinclair Award for Sustained Excellence in Aerosol Research awarded by the American Association for Aerosol Research.

Dr. Chunsheng Wang is an Associate Professor in the Chemical and Biomolecular Engineering at the University of Maryland. He received his Ph.D. from Zhejinag University, China in Materials Science and Engineering. Prior to joining University of Maryland in August, 2007, he was an assistant professor in Department of Chemical Engineering at Tennessee Technological University (TTU) from 2003 to 2007 and a Research Scientist in Center for Electrochemical System and Hydrogen Research at Texas A&M University from 1998 to 2003. His research focuses on Li-ion batteries and fuel cells.